The single-pair unwrapping ceiling is a property of the track, not of the radar

Projected sensitivity at four Sentinel-1 geometries over two rock–ice avalanche sources, with the optical detection floor measured alongside

Prepared 17 September 2026

Ajay Kumar Sah
Purbanchal University School of Engineering, Biratnagar, Nepal
ajayshah2005@gmail.com
ORCID: https://orcid.org/0009-0004-8543-4306

NON-PEER-REVIEWED PREPRINT. This manuscript is a non-peer-reviewed preprint submitted to EarthArXiv. It has not been submitted to a journal for peer review.

Companion to: Sah, A. K. (2026) *No detectable precursor in Sentinel-1 backscatter before the 26 August 2026 Langtang Lirung rock–ice avalanche, Nepal.* EarthArXiv, doi:10.31223/X59N5N. Sah, A. K. (2026) *Calibrated detection limits in routine Sentinel-1 products 50.6 hours before the Langtang Lirung rock–ice avalanche, Nepal.* EarthArXiv, doi:10.31223/X5KZ3G. Sah, A. K. (2026) *Bounded at both ends: the detection window of routine 12-day C-band InSAR at rock–ice avalanche sources.* EarthArXiv, doi:10.31223/X58J72.

Analysis code, derived data and the verification script are archived at Zenodo, doi:10.5281/zenodo.22541071, which resolves to the latest version of that record. The version accompanying this paper is 6.0.0. Contains modified Copernicus Sentinel data 2017–2026.

Abstract

The half-fringe limit of a repeat-pass interferogram is quoted as a property of the sensor: a quarter wavelength of line-of-sight displacement per pair. On a slope it is not. Sensitivity to downslope motion is $f = |m \cdot u|$, and at a mountain source f varies with the track, with the site, and across the source itself. We compute f per pixel over 500 m source discs at two rock–ice avalanche sources, Langtang Lirung (Nepal, 2026) and Ronti Peak (India, 2021), on four Sentinel-1 relative orbits, from a 30 m DEM, look azimuths measured from product footprints, and incidence angles measured directly from on-demand interferometric products. Expressed as a downslope rate, the single-pair ceiling is 0.46 m yr^{-1} on Langtang descending and 2.77 m yr^{-1} on Langtang ascending: a factor of 6.0 between two geometries of the same sensor, over the same source, in the same week. At Ronti the same comparison gives 1.25. How track-dependent the ceiling is, is itself site-dependent. Within a single 500 m disc, f spans 1.3× on Langtang descending and 13.6× on Langtang ascending, so on most geometries the ceiling is not a value for the source but a distribution across it. This accounts physically for a result previously reported as an empirical curiosity — that the best-covered geometry measures worst — because near-normal incidence is simultaneously the condition for full coverage, for insensitivity to downslope motion, and for the widest internal spread in sensitivity. We then measure the other instrument's limit at the same source: the detection floor of single-pair optical pixel-offset tracking, from 28 Sentinel-2 pairs against a prespecified stable-ground control. That floor does not improve with separation ($\sigma \sim T^{0.25}$) and is set instead by scene-pair condition, which the quantity most easily computed before processing, tile cloud cover, fails to predict. Joint screening on snow and cloud over the source area halves the spread and halves the median floor, and roughly doubles the number of pairs in which a published pre-failure rate of 9.6 m yr⁻¹ downslope would have been detectable. The floor reproduces at the second site, 5.77 against 5.55 m yr⁻¹, once pairs spanning that site's own failure are removed — those decorrelate the control area itself, at twenty-five times the dispersion of a same-separation pair that does not span it. Neither instrument detects the published rate in a single routine product on any geometry examined. A null from a 12-day pair is uninterpretable without the projected ceiling for that specific track, and λ/4 is not sufficient.

---

1. Introduction

A repeat-pass interferogram cannot unambiguously measure more than half a fringe of displacement between adjacent pixels. For Sentinel-1 at 55.46 mm this is 13.87 mm of line-of-sight motion per pair, or 0.42 m yr⁻¹ at a 12-day repeat. The number is quoted as if the sensor fixed it.

It does not. An interferogram measures the projection of ground motion onto the radar line of sight, and at a mountain source the quantity of interest is not line-of-sight motion but downslope motion. The projection factor between them depends on the local incidence angle and on the azimuth between the look direction and the slope aspect. Both vary between tracks over the same target, and both vary across a single source.

This matters because nulls are reported at these sources without it. In three companion studies we found no detectable precursor in Sentinel-1 backscatter at Langtang Lirung (Sah 2026a), measured a calibrated detection floor 50.6 hours before failure (Sah 2026b), and showed that no published precursory detection we could find lies inside the range a single 12-day pair can measure (Sah 2026c). That last study also reported, without explaining, that at Langtang the ascending track covering 100 per cent of the source disc has about four times the variance of a descending track covering 44 per cent (4.1× on the underlying measurement), and misses the failure entirely (z = −0.52) where the descending track registers it at z = +3.43.

Independently, Wang et al. (2026) report over 100 m of pre-failure deformation at the same source from optical pixel-offset tracking, with an acceleration beginning January 2026. Two instruments, the same slope, opposite outcomes. The natural question is where each instrument's measurable range actually sits at a real source, rather than at the nominal sensor specification.

This study answers that for four Sentinel-1 geometries at two sites, and then measures the optical floor at one of them.

2. Data

DEM. Copernicus GLO-30, tiles N28 E085 and N30 E079, read directly from the AWS open bucket.

Source discs. Langtang Lirung 28.2853 N, 85.5252 E; Ronti Peak 30.37775 N, 79.72698 E; radius 500 m, as in Sah (2026c). GLO-30 gives a disc-mean aspect of 280.5° at Langtang against the 281.8° verified independently in that study, a 1.3° agreement that validates the DEM route.

Local incidence angles. Disc medians published in Sah (2026c), Figure 1: 71.0° (Langtang descending, relative orbit 19), 22.6° (Langtang ascending, r.o. 85), 45.0° (Ronti r.o. 63), 51.3° (Ronti r.o. 165).

Look azimuths. Measured from the range edges of real product footprints retrieved from the ASF catalogue: 280.9° descending, 80.3° ascending. Nominal values from published headings are 282.5° and 77.5°, agreeing to 1.6° and 2.8°.

Track identity. Sah (2026c, §2.3) records that selecting a Ronti track by orbit direction alone produced a misattributed geometry measurement, because both descending tracks pass within eight minutes of each other — relative orbit 63 at approximately 00:43 UTC and relative orbit 165 at approximately 00:35. Every product used here was checked against that signature: the r.o. 63 granule acquires at 00:43:44 and the r.o. 165 granule at 00:35:34. Relative orbit is used as the key throughout, never the frame number, which Sah (2026c) shows is not stable across years.

Optical. Sentinel-2 L2A band B04 (red, 10 m), MGRS tile 45RUM, from the AWS `sentinel-cogs` open bucket via the Earth Search STAC API. One scene per year 2018–2025 for the floor measurement; 140 candidate scenes screened.

2.1 Use of AI-assisted technology

The analysis code used to produce the results and figures reported here, and the initial drafting of this manuscript, were produced with assistance from Claude (Anthropic), a large language model, in interactive sessions during September 2026. The model was used to write the processing and statistical code, to generate the figure, to check the cited literature against primary sources, and to draft text. All satellite data acquisition and export, the choice of sites, tracks and acquisition dates, the submission of the on-demand products, and the interpretation of results are the author's.

Three points specific to this manuscript. The control design of §5.1 was prespecified before any pair was scored, and is archived unchanged. Two errors made during the assisted sessions are reported in §3.2 and not removed, together with the signatures by which each was detected; both are checked by the verification script. And the incidence angles of Table 1a were measured rather than inferred after an earlier bound, though correct, was found to be uninformative on one geometry — that sequence is reported in §3.1 and not presented as a single confident measurement.

The author has verified the reported values by running the accompanying verification script, which re-derives every measured quantity in Section 4 from freely available source data and reports 52 checks passed. The author accepts full responsibility for the content.

3. Method

For each DEM pixel we compute slope β and aspect A, then the upward surface normal

```
n = [sin A sin β, cos A sin β, cos β]
```

and the downslope unit vector

```
m = [sin A cos β, cos A cos β, −sin β]
```

The ground-to-satellite unit vector for a right-looking sensor with look azimuth α and incidence θ is

```
u = [−sin θ sin α, −sin θ cos α, cos θ]
```

The local incidence angle is arccos(n · u), and the sensitivity of the line of sight to downslope motion is f = |m · u|. The single-pair ceiling expressed as a downslope rate is ($\lambda/4$ per pair, annualised) divided by f.

θ is not directly available without an authenticated product download. We therefore sweep it across the Sentinel-1 IW range, 29–46°, and admit only those values for which the modelled disc-median local incidence angle lands within 2° of the median published in Sah (2026c). This uses a measurement made for a different purpose as a calibration, and it constrains θ tightly on three of the four geometries.

3.1 The incidence angle, measured

θ was measured for all four geometries rather than bounded. Four on-demand HyP3 INSAR_GAMMA jobs, one per relative orbit, submitted with the incidence-map and look-vector options enabled, return an ellipsoid incidence raster. Over the 500 m discs these give 33.92°, 40.10°, 34.39° and 45.73°, each varying by less than 0.07° across the disc — as expected for a terrain-independent quantity, and a useful check that the product is what it claims to be. A further consistency check: 90° − `lv_theta` gives 40.30° for the ascending track against 40.10°.

The bounding method was correct on all four, and uninformative on one. Every measured θ falls inside the range the published LIA median admitted: 33.92 within 32.2–37.8°, 34.39 within 31.0–37.8°, 45.73 within 41.5–46.0°. On Langtang ascending the median admitted the entire IW range, because at near-normal incidence the disc-median local incidence barely responds to θ. The bound contained the answer everywhere and narrowed it in three cases out of four. The case where it failed to narrow is the one where the measurement mattered most, since the measured 40.10° sits near the end of the admitted range, the end yielding the largest ceiling.

This is worth stating plainly rather than presenting the bound as vindicated. A bound that is correct but uninformative is not the same as a bound that works, and which of the two you have cannot be judged from the bound itself.

3.2 Two errors, both silent

Both are reported because both produce plausible output.

A surface normal tilted *away from* rather than *toward* the downslope direction reproduces the published local incidence medians **exactly swapped** between ascending and descending. Predicted values of 1.4° and 76.8° against measured 71.0° and 22.6° are not a small residual; they are the right numbers on the wrong geometries, which is the signature to look for.

Second, the convenient approximation f ≈ sin(LIA)·cos(Δaz), which would eliminate θ entirely, is accurate at grazing incidence and fails at near-normal incidence. On Langtang descending it matches the exact projection to about 0.03; on ascending the error reaches 0.12 and the approximation moves in the wrong direction as θ changes. The reason is physical: near normal incidence the in-plane direction of the look vector is poorly determined. θ cannot be eliminated this way.

4. Results: the radar ceiling

The four geometries are set out below in two parts. Table 1a gives the measured incidence angle for each track and the local incidence angle that follows from it, against two sources that measured the same quantity independently. Table 1b gives the sensitivity to downslope motion and the single-pair ceiling it implies.

Table 1a. Incidence angle, measured, and the local incidence it implies — against two independent sources.

site	geometry	θ measured	LIA modelled	LIA HyP3	LIA published
Langtang	desc. r.o. 19	33.92°	70.70°	71.42°	71.0°
Langtang	asc. r.o. 85	40.10°	21.79°	21.46°	22.6°
Ronti	desc. r.o. 63	34.39°	44.81°	44.33°	45.0°
Ronti	desc. r.o. 165	45.73°	52.32°	50.66°	51.3°

Table 1b. Sensitivity to downslope motion and the resulting single-pair ceiling, per pixel over the 500 m disc.

site	geometry	f (p50)	ceiling, m yr^{-1}	f spread, p90/p10
Langtang	desc. r.o. 19	0.914	0.46	1.3×
Langtang	asc. r.o. 85	0.153	2.77	13.6×
Ronti	desc. r.o. 63	0.437	0.97	4.7×
Ronti	desc. r.o. 165	0.349	1.21	10.0×

The three local-incidence columns come from three independent chains: this work's projection from Copernicus GLO-30, HyP3's GAMMA processing on its own DEM, and the Copernicus Browser evalscript used in Sah (2026c). Twelve values, worst disagreement 1.7°, most under one degree.

As a by-product this independently reproduces Figure 1 of Sah (2026c) on a different processor: 71.42 against 71.0, 44.33 against 45.0, 50.66 against 51.3, and 21.46 against 22.6.

4.1 The ceiling is a property of the track

Between the two Langtang geometries the ceiling differs by a factor of 6.0. Same sensor, same source, same week. Quoting λ/4 as a single number conceals a factor of several.

4.2 How track-dependent it is, is a property of the site

At Ronti the two available descending tracks differ by only 1.25 times. The between-track spread is not a constant of the technique. This extends the central finding of Sah (2026c) — that the bounds of the detection window are site-specific — to a quantity that had not previously been examined.

The Ronti tracks share a look azimuth and differ only in incidence — 34.39° and 45.73° measured, near and far swath respectively. That is why they behave so similarly and the two Langtang tracks so differently: Langtang's pair look from opposite sides, Ronti's from the same side at different ranges.

4.3 Within a single source the ceiling is a distribution

On Langtang descending, f varies by a factor of 1.3 across the 500 m disc, from 0.734 at the 10th percentile to 0.989 at the 90th: the ceiling is effectively one number. On Langtang ascending it varies by 13.6 times, 0.032 to 0.431, and on the two Ronti tracks by 4.7 and 10.0. On three of four geometries different parts of the same source face have unwrapping limits close to an order of magnitude apart, and on the ascending track the quantity is not usefully summarised by a median at all.

4.4 Why the best-covered geometry measures worst

Sah (2026c) reported that the Langtang ascending track covers the whole source disc, has about four times the variance of the descending track, and does not register the failure. The projection accounts for that result.

Near-normal incidence produces all three effects at once. It gives complete coverage with no shadow, because the beam reaches every facet. It gives low sensitivity to motion lying in the surface plane, because the line of sight is close to the surface normal. And it gives the widest internal spread in sensitivity, because f depends on the angle between the look vector and the local surface, which varies most when that angle is small. Usable-pixel fraction, the quantity available before any processing, therefore selects against measurement capability on this slope.

5. Results: the optical floor at the same source

The radar ceiling is only half of what determines whether a slope is observable. The other instrument reported to have seen this deformation is optical pixel offset tracking, and its limit is a floor rather than a ceiling. We measure that floor at the same source, using the same source discs, so the two limits can be placed on one axis.

5.1 Control design

A stable-ground control was prespecified before scoring (supplementary `prespec_pot_control.md`). A node enters the control if and only if it is off the ITS_LIVE land-ice mask; at least 1000 m from the collapse marker and 500 m outside the measurement area; on GLO-30 slope between 15° and 55°; above the scene 10th percentile in patch mean reflectance in both scenes; and above the scene 25th percentile in patch standard deviation in both. No criterion refers to the displacement field. The floor is the 68th percentile of |displacement| over the control. Populations are 400–510 nodes per pair.

Correlation is by Hann-tapered phase correlation on 128 × 128 px patches with 20× upsampling. All scenes at a site share one MGRS grid, so **no raster is resampled or interpolated at any point** — a precaution taken because interpolating a raster before applying a fixed threshold biased every value in an earlier study in this programme, by 1.9 to 7.4 points, and compressed the variance by a fifth (Sah 2026c, §6.1). Read windows are padded to 900 m around a 500 m disc, giving 489 disc pixels at 40 m posting; an 800 m window truncates the disc to 484 and shifts the mean, which is the same study's other documented trap. Residual global offsets after alignment are 0.15–0.30 px.

A positive control is available in the same scenes: a glacier box 0.9–1.5 km east of the source returns 13.5–18.1 m yr^{-1}, against approximately 14.7 m yr^{-1} from ITS_LIVE autoRIFT at 120 m over the same box.

5.2 The floor does not fall with separation

Across 28 pairs built from one scene per year, 2018–2025, σ scales as $T^{0.25}$. There is no useful dependence on separation. A five-year pair can outperform a one-year pair by an order of magnitude, and a single six-year pair failed the control outright (p68 15.3 m, p95 384 m), so no floor is claimed from it.

This is why multi-epoch inversion over a redundant network of short pairs, as used by Wang et al. (2026), is not merely a refinement but a requirement.

5.3 What sets it, and what fails to predict it

Table 2. Same correlator, same control, same 28-pair design; only scene selection differs.

scene selection	median σ	spread	median rate floor	pairs detecting 9.6 m yr^{-1}
tile cloud cover < 10 %	13.03 m	42×	11.60 m yr^{-1}	11 of 28
AOI snow fraction alone	32.13 m	81×	30.30 m yr^{-1}	—
AOI snow + 2 × AOI cloud	12.47 m	19×	5.55 m yr^{-1}	20 of 28

Snow fraction over the source area spans 13.8 to 79.8 per cent within a single October–December window at under 10 per cent tile cloud, so the metric in common use does not constrain it. Selecting on snow alone is worse than not selecting, because the least-snowy scene in a season is often the cloudiest over the source: the

2019 minimum-snow scene carries 23.6 per cent cloud over the area of interest, and every pair containing it exceeds σ = 130 m.

This is the optical counterpart of Section 3.1 of Sah (2026c). There, radar viewing geometry could not be selected on usable-pixel fraction, the quantity most easily computed before processing. Here, optical pairs cannot be selected on tile cloud cover, the quantity most easily computed before processing. The same failure mode appears in both instruments.

5.4 The same measurement at Ronti, and a second failure mode

The design of Section 5.1 was repeated at Ronti Peak: same correlator, same control criteria, one Sentinel-2 scene per year 2018–2025 screened on snow and cloud over the source area, with a hard cap of 5 per cent area cloud, 28 pairs, 400–640 control nodes each.

Taken as a whole the Ronti set looks worse than Langtang — median σ 12.96 m against 12.47 m, but a spread of 76× against 19×, and a median rate floor of 11.67 against 5.55 m yr^{-1}. Sorting the pairs by whether they span the 7 February 2021 failure resolves it completely.

Ronti, 28 pairs	n	σ min	σ median	σ max	median rate floor
spans the failure	15	9.74 m	91.99 m	170.75 m	54.75 m yr^{-1}
does not span it	13	2.24 m	4.92 m	11.69 m	5.77 m yr^{-1}

This split was made after the 28 pairs were scored, not before. It is therefore post-hoc, and post-hoc subsetting has produced at least one retracted finding in this programme. Three things distinguish it from that case. The partition is on a date fixed by the event and known independently of any measurement, not on the values themselves. It divides the set almost evenly, 15 against 13, rather than isolating a small tail. And the effect is a factor of nineteen in the median, not a marginal shift. The finding is reported on that basis, and a prespecified test of it would require a third site.

Separation does not explain the split. The decisive comparison is 2020→2021, which spans the failure at 1.11 yr separation and gives σ = 122.50 m, against 2021→2022, which does not span it at 1.05 yr and gives σ = 4.92 m: the same separation and twenty-five times the dispersion.

The event decorrelates its own control area. The control excludes everything within 1000 m of the source, but the 2021 Chamoli flow scoured the valley for tens of kilometres, so terrain change reaches far outside any plausible source buffer. A control defined by distance from the source is not sufficient at a site that has failed; it must also be checked for event-related change.

And once those pairs are removed, the two sites agree. The floor is 5.55 m yr^{-1} at Langtang across 28 pre-event pairs and 5.77 m yr^{-1} at Ronti across 13 non-spanning pairs. The spread is narrower at Ronti, 5× against 19×. The floor measured in Section 5.3 is therefore not a Langtang peculiarity.

5.5 Reconciling this floor with the one reported in Sah (2026c)

Sah (2026c, §3.4) places the two techniques' usable ranges close together: a half-fringe ceiling of 0.42 m yr^{-1} against a pixel-offset precision of 0.47 m yr^{-1}, taken from Li et al. (2025), who give about one-thirtieth of a 2.33 m range pixel at a 60-day baseline. That paper concludes the ranges are nearly contiguous. The floor measured here is an order of magnitude higher, and the difference needs stating, since the two papers would otherwise appear to disagree.

Expressed in pixels the two are not comparable quantities. Li et al. report 0.033 px; the single pairs measured here give 0.21 px at best and 1.25 px at the median, on a 10 m pixel. That is six to thirty-seven times coarser in pixel units, and the sensor is not the reason.

Two things separate them. Li et al. report a post-inversion precision over a redundant network of pairs, which is what SBAS delivers; this study reports the dispersion of a single pair, deliberately, because the question is what one routine product contains. And their target is fast, well-textured glacier surface, where correlation is easy, against the mixed rock and seasonal snow of a control population here.

Both numbers are correct for what they describe. Read together they say that the floor of pixel-offset tracking, like the ceiling of interferometry, is not a property of the technique: it varies by more than an order of magnitude with the processing chain and the surface. The contiguity reported in Sah (2026c) holds for an inverted stack on clean ice. It does not hold for a single pair on a mixed source disc, which is the case examined here.

6. Neither instrument, in a single pair

Wang et al. (2026) report 7.4 m yr^{-1} horizontal at this source before January 2026, which is 9.6 m yr^{-1} downslope at the measured slope of 39.7°.

This value is read from their Figure 2, not from a table or from text. It is the only quantity in this study taken from a figure rather than measured or quoted from a numeric statement. It is used here for scale — to establish the order of magnitude by which the published rate exceeds the ceilings in Table 1b — and no conclusion depends on its third significant figure. At 5 m yr^{-1} or 15 m yr^{-1} the argument of this section is unchanged. That rate exceeds every C-band ceiling in Table 1 by factors of 3 to 21. It sits above the median single-pair optical floor under common-practice scene selection and below it under joint screening.

So the deformation reported at this source is not detectable in a single routine product of either kind, on any geometry examined here, under scene selection as usually practised. It became detectable through multi-epoch inversion. The null reported in Sah (2026a, 2026b) was structural rather than a processing failure, and the size of the structural margin is now quantified.

7. Recommendation

Report the projected ceiling for the specific track, not λ/4. It is computable before any processing, from a public DEM and the orbit geometry, at no cost. Where the sensitivity varies materially across the source, report its distribution rather than its median.

For optical pair selection, screen on snow and cloud over the source area rather than on tile cloud cover.

8. Limitations

All four incidence angles are measured (Section 3.1), so no geometry in Table 1 rests on a bound. The look azimuths remain measured from product footprints rather than from orbit state vectors, an approximation good to a degree or two at these latitudes.

Slope β at Langtang is taken from the pre-failure surface, which is partly ice-covered. It affects Section 5 and Section 6 only, not Section 4.

The floor reported in Section 5 is a single-pair dispersion and is not comparable with a post-inversion precision; Section 5.5 sets out why, and why it does not contradict Sah (2026c, §3.4).

Section 5 rests on one season at each site. The floor now has two-site support (Section 5.4), but the three-way scene-selection comparison of Table 2 was run at Langtang only; whether tile cloud cover fails as a selection metric at Ronti in the same way is untested.

Figures

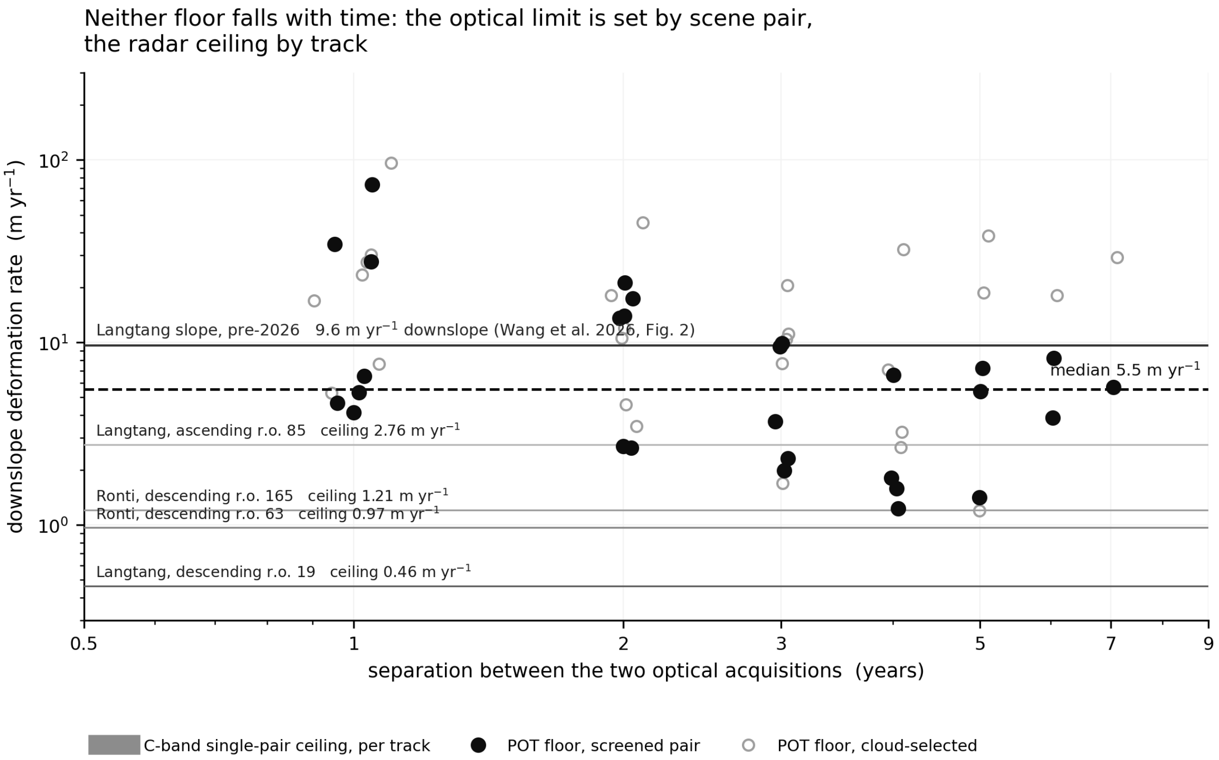

Figure 1. The two instruments' limits at these sources, on one axis. Vertical axis is downslope deformation rate, horizontal axis the separation between the two optical acquisitions, both logarithmic. The four horizontal bands are the single-pair C-band unwrapping ceilings of Table 1b, one per relative orbit, computed per pixel from Copernicus GLO-30 with incidence angles measured from HyP3 `inc_map_ell` products. They are horizontal because a single-pair ceiling does not depend on separation. Filled circles are the optical pixel-offset detection floor measured here, one per Sentinel-2 pair, under joint snow-and-cloud screening; open circles are the same 28 pairs selected instead on tile cloud cover, the criterion in common use. The dashed line is the median of the screened set, 5.5 m yr^{-1}.

The optical points scatter flat: the floor does not improve with separation ($\sigma \sim T^{0.25}$, §5.2). The horizontal line at 9.6 m yr⁻¹ is the published pre-2026 rate at Langtang expressed downslope. It sits above every radar ceiling by factors of 3 to 21, and within the optical scatter rather than above it: under good screening most pairs would have detected it, under common practice most would not, and no single C-band pair on any of the four tracks could have.

Data and code availability

Analysis code, derived data and verification scripts are archived at Zenodo, doi:10.5281/zenodo.22541071 (concept DOI; use the latest version).

References

All DOIs resolved and metadata confirmed 17 September 2026; see `references_verified_paper4.md`.

Bontemps, N., Lacroix, P., Doin, M.-P. (2018) Inversion of deformation fields time-series from optical images, and application to the long term kinematics of slow-moving landslides in Peru. *Remote Sensing of Environment* **210**, 144–158. doi:10.1016/j.rse.2018.02.023

Guo, L. et al. (2026) Progressive entrainment transformed a high-elevation ice–rock avalanche in Nepal into the 26 August debris flow in Gyirong, Xizang. *Chinese Science Bulletin*. doi:10.1360/CSB-2026-1255

Li, H., Yang, Y., Dong, X., Xu, Q., Li, P., Zhao, J., Chen, Q., Hu, J.-C. (2025) Frequent glacial hazard deformation detection based on POT-SBAS InSAR in the Sedongpu Basin in the Himalayan region. *Remote Sensing* **17**(2), 319. doi:10.3390/rs17020319

Leprince, S., Barbot, S., Ayoub, F., Avouac, J.-P. (2007) Automatic and precise orthorectification, coregistration, and subpixel correlation of satellite images. *IEEE Transactions on Geoscience and Remote Sensing* **45**, 1529–1558. doi:10.1109/TGRS.2006.888937

Sah, A. K. (2026a) No detectable precursor in Sentinel-1 backscatter before the 26 August 2026 Langtang Lirung rock–ice avalanche, Nepal. EarthArXiv. doi:10.31223/X59N5N

Sah, A. K. (2026b) Calibrated detection limits in routine Sentinel-1 products 50.6 hours before the Langtang Lirung rock–ice avalanche, Nepal. EarthArXiv. doi:10.31223/X5KZ3G

Sah, A. K. (2026c) Bounded at both ends: the detection window of routine 12-day C-band InSAR at rock–ice avalanche sources. EarthArXiv. doi:10.31223/X58J72

Shugar, D. H. et al. (2021) A massive rock and ice avalanche caused the 2021 disaster at Chamoli, Indian Himalaya. *Science* **373**(6552), 300–306. doi:10.1126/science.abh4455

Van Wyk de Vries, M., Bhushan, S., Jacquemart, M. et al. (2022) Pre-collapse motion of the February 2021 Chamoli rock–ice avalanche, Indian Himalaya. *Natural Hazards and Earth System Sciences* **22**, 3309–3327. doi:10.5194/nhess-22-3309-2022

Wang, T., Sassa, S., Yang, W., Li, R., Xu, C., Qi, W. (2026) Precursor of a powerful large glacier landslide causing tsunami floods in the 26 August 2026 Nepal disaster. *Landslides*. doi:10.1007/s10346-026-02842-6

Data availability

Copernicus GLO-30 DEM (ESA/Airbus), tiles N28 E085 and N30 E079, from the AWS `copernicus-dem-30m` open bucket. Sentinel-2 L2A from `sentinel-cogs` via the Earth Search STAC API, MGRS tiles 45RUM and 44RLU. ITS_LIVE annual velocity composites (NASA MEaSUREs), `v2-updated-september2025`. Four HyP3 INSAR_GAMMA products from the Alaska Satellite Facility, 10×2 looks, with the incidence-map and look-vector options enabled.